Michigan Technological University

Digital Commons @ Michigan Tech

Michigan Tech Publications

2-2022

3D-printed polycaprolactone-chitosan based drug delivery implants for personalized administration

Yutong Yang
Northeast Forestry University

Haichao Wu
Northeast Forestry University

Qiliang Fu
SCION

Xinfeng Xie
Michigan Technological University, xinfengx@mtu.edu

Yongming Song
Northeast Forestry University

See next page for additional authors

Recommended Citation

Yang, Y., Wu, H., Fu, Q., Xie, X., Song, Y., Xu, M., & Li, J. (2022). 3D-printed polycaprolactone-chitosan based drug delivery implants for personalized administration. *Materials and Design, 214*. http://doi.org/10.1016/j.matdes.2022.110394
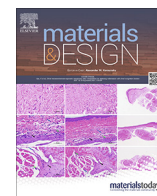Retrieved from: https://digitalcommons.mtu.edu/michigantech-p/15666

Authors

Yutong Yang, Haichao Wu, Qiliang Fu, Xinfeng Xie, Yongming Song, Min Xu, and Jian Li

3D-printed polycaprolactone-chitosan based drug delivery implants for personalized administration

Yutong Yang [a,1], Haichao Wu [a,1], Qiliang Fu [b], Xinfeng Xie [c], Yongming Song [a,*], Min Xu [a], Jian Li [a]

[a] Key Laboratory of Bio-based Material Science and Technology (Ministry of Education), Northeast Forestry University, Harbin 150040, PR China
[b] Scion, 49 Sala Street, Rotorua 3020, New Zealand
[c] College of Forest Resources and Environmental Science, Michigan Technological University, Houghton, MI 49931, USA

HIGHLIGHTS

- Polycaprolactone and water-soluble chitosan were combined in 3D-printed drug delivery implant for sustained-release.
- All the materials of the 3D-printed implant are biocompatible, biodegradable, low-toxic, cost-effective, renewable, and the method is simple and green.
- The preparation process was carried out below 120 °C and solvent-free to maintain the drug activity.
- Sustained release reached 99% and lasted for 120 h by tailoring the drug and chitosan content of the 3D-printed implant.

GRAPHICAL ABSTRACT
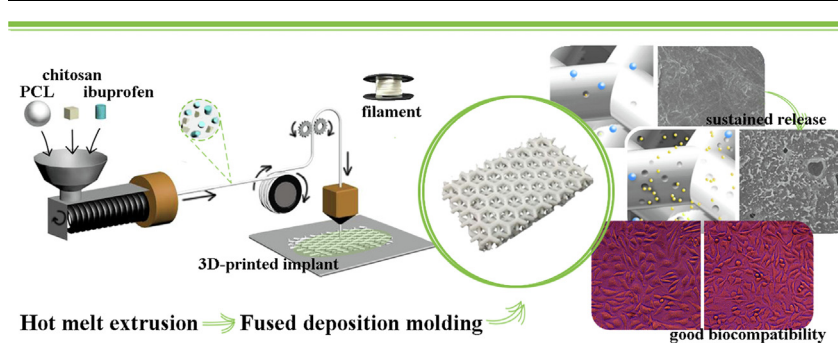
ABSTRACT

Fused deposition molding (FDM) can complete most complex preparation of drug delivery implants to meet the personalized needs of patients. However, the drug activity has strict requirements on processing temperature and preparation method of filaments, the implant also has strict biocompatibility requirements for the materials. In this study, a drug delivery implant was prepared with good biocompatibility, controlled and efficient drug release using FDM printing for personalized administration. Drug-loaded filaments were developed for FDM process by hot-melt extrusion (HME). Polycaprolactone was used as a drug delivery carrier, and ibuprofen as the model drug. Notably, chitosan was dissolved to form controlled and efficient release channels. The printability, changes in physical and chemical properties during HME and FDM processes of the filament, and drug release behavior, mechanism and biocompatibility of the implants were investigated. The results showed that the filament tensile strength decreased with the increase of drug and chitosan content. No obvious degradation and chemical change occurred during the whole process. The drug release efficiency could reach>99% and lasted for 120 h mainly via the diffusion - erosion mechanism. The viability of cells cultured for 24 h in 72 h, 100% implant extract was 75.3%.

1. Introduction

In recent years, personalized drug delivery has generated a lot of interest owing to the outstanding treatment results [1]. Personal drug delivery meets the needs, characteristics, and preferences of each patient, and hence exploring its administration methods is of great significance [2]. A good drug administration route should possess a relatively high transport efficiency of drugs, reduce the toxicity and side effects of systemic or local administration, and minimize the discomfort of patients during administration. The commonly used drug delivery methods, including intravenous injection, oral administration, makes the drug concentration in blood rise rapidly in a short time, the concentration of the drug taken orally also reduces greatly through the liver [3,4]. Therefore, it is difficult to maintain the drug concentration in a therapeutically relevant range under the premise of one-time administration through traditional drug delivery methods. While implants loaded with active pharmaceutical ingredients (API) can accurately deliver the drug to the target site and maintain the drug concentration, improve drug delivery efficiency, reduce administration frequency and improve compliance, ultimately improve the clinical results of patients significantly [5]. In addition, the implant can be manufactured as a scaffold or catheter to support the damaged part, promote the rehabilitation of the injury [6–8]. However, it is difficult to manufacture such novel drug implants with complex shapes to fit the injury using conventional processing methods.

It is well recognized that three-dimensional (3D) printing can address most manufacturing issues; of all the systems, fused deposition modeling (FDM) is one of the most widely used in healthcare [5,9,10]. FDM is an extrusion-based "bottom-up" process that involves the layer-by-layer addition of a material. It is flexible, and customizable, and has a simple operation [11]. The equipment of FDM mainly includes an actuating device, which allows the polymer filament to proceed through the nozzle where the polymer is melted and then immediately cooled and deposited in the plane or building model [12]. Polymeric materials with good biocompatibility have been widely used for *in vitro* cell cultures [13,14], tissue engineering scaffolds [15,16], and drug delivery systems [17–19], which show potential for integration with 3D-printed drug delivery implants.

In general, polymers with certain rigidities, strengths, flexibility, melt flow characteristics, and good crystallinity are suitable for FDM process. Previously reported common sustained-release polymer matrices include poly (vinyl alcohol) [20], ethylene–vinyl acetate copolymers [21], polylactic acid [22] and Kollidon®VA64, Kollicoat® IR [23], Eudragit RL [24], (poly(lactic-co-glycolic acid) [25], which can withstand the relatively high processing temperatures of FDM. Nevertheless, a risk of inactivating APIs at such high processing temperatures exists, and the biocompatibility of materials should be considered. Thus, it is crucial to select a suitable polymer matrix for preparing of drug delivery implants using FDM. Polycaprolactone (PCL) is a polymer with a low melting point. It is approved by the Food and Drug Administration (FDA) as a bioabsorbable suture and drug delivery biomaterial due to its nontoxicity, good biocompatibility, excellent flexibility, and degradability [26,27], which make it suitable for use as a drug delivery implant [27,28]. However, there are few studies on 3D-printed PCL as drug sustained release carrier. Meanwhile, the drugs are tightly embedded once added into the polymer matrix, making their release through diffusion difficult [29]. To address this issue, previous studies add some natural polymers, such as chitosan (CS), hydroxypropyl cellulose and/or gelatin to the matrix as release modifiers to render it flexible with controlled drug release [30–32]. There are studies on adding CS to PCL for 3D printing. However, their research focuses on the mechanical properties, biological response of the final product. The effects of drugs were not taken into accounts, thus the drug sustained-release performance have not been explored [33,34]. Besides the selection of polymers, it is necessary to prevent the blockage of the nozzle by large particulates during FDM process. An organic solvent is usually introduced to ensure that the mixture is more uniform for printing. However, the addition of the solvent may affect the activity of the drug [35,36].

This study aimed to prepare the drug-loaded PCL-CS filament by hot-melt-extrusion (HME) process without adding the solvent, and then construct a drug delivery implant with a sustained drug release function using FDM process. Ibuprofen (IBP), a non-steroidal anti-inflammatory drug, also possesses analgesic and antipyretic activity. It can be used as the model drug to manufacture unconventional and effective polymer drug binding systems [37,38]. Water-soluble CS was added to the insoluble matrix to form release channels and realize the controlled and efficient release of drugs. PCL was used as a drug delivery carrier to obtain a low processing temperature and prevent reductions in drug activity. We investigated the printability, physical and chemical changes during HME and FDM processes of the filament, biocompatibility, drug release behavior and mechanism of the implants.

2. Materials and methods

2.1. Materials

Polycaprolactone (PCL, CAPA6800; M_n = 80,000, d = 3 mm, melt index (MI) = 0.74 g/10 min (100 °C/2.16 kg)) was obtained from Solvay Co., Ltd. (Guangdong, China). Ibuprofen (IBP) was ordered from Beilang Biotechnology Co., Ltd. (Shanghai, China). Chitosan (CS, Mv = 1000, Deacetylation degree $\geq$ 95%) was purchased from Gubei Biotechnology Co., Ltd. (Jiangsu, China). Phosphate-buffered saline (PBS, XY-4308-1) solution with pH of 7.4 was acquired from Meilun Biotechnology Co., Ltd. (Dalian, China). Minimum Essential Medium (MEM) and fetal bovine serum were ordered from Hyclone (Logan, USA), trypsin and penicillin streptomycin were provided by Biosharp (Anhui, China), L-929 cell, methyl thiazolyl tetrazolium (MTT) assay kit were purchased from Beijing solarbio science & technology Co., Ltd. (Beijing, China). Isopropanol was provided by Aladdin (Shanghai, China). HDPE (5420 GA, melt index (MI) = 2.3 g/10 min (190 °C/ 21.6 kg), 0.95 g/cm^3) was purchased from the PetroChina Co. Ltd. (Beijing, China).

2.2. Preparation of filaments

PCL, IBP, and CS were dried in a vacuum oven at 40 °C for 24 h to remove moisture. The dried materials were weighed in different proportions (Table 1) and mixed in a high-speed blender for 5 min. The mixture (300 g) was placed in a mini conical twin-screw extruder (JZSZ–10A, Wuhan Ruiming Experimental Instrument Manufacturing Co., Ltd., China) for HME and granulation. The extrusion temperatures were set at 105 °C and 120 °C, and the screw rotation speed was fixed at 25 rpm. After granulation, the extrudates were dried under vacuum at 40 °C for 24 h. The extrudates were passed through a single-screw extruder (the barrel temperature from the feeding position to the die was 100 °C, 105 °C, 105 °C, and 100 °C, and the screw rotation speed range was 220 – 240 rpm). To precisely control the filament diameter, a laser diameter gauge was used to monitor whether the filament diameter was within the standard range in real time and adjust the screw speed and pulling speed according to the feedback of the measurements. The final filaments with diameters of about 1.75 ± 0.05 mm were extruded.

Table 1
Composition of the filaments for HME.

Sample	PCL (%, w/w)	IBP (%, w/w)	CS (%, w/w)
PCL	100	–	–
PC5I4	91	4	5
PC5I8	87	8	5
PC5I12	83	12	5
PC5I16	79	16	5
PC5I20	75	20	5
PI12C4	84	12	4
PI12C8	80	12	8
PI12C12	76	12	12
PI12C16	72	12	16
PI12C20	68	12	20

2.3. Mechanical properties of filaments

The tensile strength of the filaments with different amounts of CS and IBP was determined using a universal testing machine (RGT-20A, REGER, China) at room temperature. The filament sample size was determined using an electronic micrometer, with a diameter d_0 of 1.75 ± 0.05 mm, a length l_0 of 140 mm, an original standard distance of 60 mm, and a tensile speed of 50 mm/min. Each experiment was repeated six times, and the mean value was reported as the final result.

2.4. Dynamic rheological analysis of filaments

The dynamic rheological tests were carried out using a rotational rheometer (AR 2000ex, TA Instruments, UK) to determine the viscoelastic properties of the filaments with different amounts of IBP and CS. Standard ETC steel parallel plates (diameter = 25 mm) were used with a 1 mm gap between the lower plate and the upper plate. The oscillating frequency sweep was from 628.3 to 0.683 rad/s, the temperature was fixed at 120 °C, and a constant strain amplitude of 0.01% was applied, which was well within the linear viscoelastic region. Each experiment was repeated three times, and the mean value was reported as the final result.

2.5. Implant preparation

A 3D model of the implant structure was designed using 3Ds Max 2018 software and then exported as an STL file. 3D slicing software was used to fill and slice the structure to obtain models with different printing parameters. As shown in Fig. 1, the different filaments prepared by HME were fed to fabricate the implants using a commercially available desktop FDM printer (Gaonuo-a001, Gaonuo-3d, China). The detail parameters of 3D printing were listed in Table 2.

2.6. Characterization

2.6.1. Fourier-transform infrared spectrometry (FTIR) analysis

Fourier-transform infrared (FTIR) spectrometry (iS10, Nicolet, USA) was used in the attenuated total reflectance mode in the range of 700–4000 cm^{-1} at a resolution of 4 cm^{-1} with 32 scans. 3D-printed implants, pure PCL, CS and IBP were tested. Three points were randomly selected on PCL, IBP, CS powder, and the implants. The average value was taken as the final result.

2.6.2. Thermal analysis

The thermal behaviors of PCL, IBP, CS, and 3D-printed implants were analyzed with a differential scanning calorimeter (DSC, Diamond, PerkinElmer, USA) equipped with a refrigerated cooling system. Under the protection of nitrogen purge gas (flow rate of 100 mL/min), 5 mg sample was placed in aluminum crucibles and heated from 0 °C to 200 °C at a scanning rate of 10 °C/min. The scanning rate was held at a constant temperature for 5 min and then cooled to 0 °C at the same rate for 5 min to eliminate the thermal history of samples. Then, the temperature was raised to 200 °C at a rate of 10 °C/min, and the second DSC curve was recorded. The voltage was 5 kV. Each experiment was repeated three times to eliminate errors.

The thermal degradation behavior was also tested using a thermal gravimetric analyzer (TGA, Q50, TA, USA). The platinum crucible was first tared, then 6 mg sample was placed in the platinum crucible. The ramp rate was 10 °C/min from 25 °C to 350 °C, under the protection of nitrogen purge gas (flow rate of 100 mL/min). The test was repeated three times.

2.6.3. X-ray diffraction (XRD)

X-ray diffraction (XRD) patterns of PCL, IBP, CS, and 3D-printed implants were obtained using an X-ray diffractometer (XRD6100, Shimadzu, Japan) with target radiation sources for Cu and Ni filters under the following conditions: a scanning range (2 theta) of 5°–50°, a scanning rate of 10°/min, a voltage of 40 kV, and a current of 40 mA. Each experiment was repeated three times to eliminate errors.

2.6.4. Micromorphology

3D-printed implants with an IBP content of 12 wt%, CS contents of 4 wt%, 8 wt%, 12 wt%, 16 wt%, and 20 wt% were observed before and after release. A scanning electron microscope (SEM; JSM-7500F, JEOL, Japan) was used to observe the microstructure of the fracture surfaces. The implant samples were brittle fractured with liquid nitrogen, and the fracture surface was sprayed with gold before SEM observations.

2.6.5. In vitro drug release

Implants with different structures and containing different amounts of the drug and CS were tested to determine the drug release behavior and mechanism in vitro, as described by Mao et al. [39], with slight modifications. The samples were dried under vacuum at 40 °C to a constant weight and accurately weighed. Then, they were soaked in 100 mL of PBS buffer (pH = 7.4) in a constant-temperature incubator with a shaking speed of 100 rpm at 37 °C. The PBS buffer was changed within a specific time. The concentration of IBP in PBS was measured with a double-beam ultraviolet–visible spectrophotometer (TU-1901, PERSEE, China). The drug concentration was measured at the characteristic absorption peak wavelength of 221 nm, and the standard curve was drawn over a concentration range of 0–1000 µg/mL, in which the drug concentration and absorbance showed a good linear relationship (R^2 > 0.999). Each group comprised three samples, and all samples were measured three times.

2.6.6. Biocompatibility

The biocompatibility was evaluated using a cytotoxicity test. According to the National Standard of China, GB/T 16886.5–2017, Mouse fibroblast L-929 was cultured in vitro to test the potential cytotoxicity of the 3D-printed implant. Firstly, the implant (PCL 80 wt%, CS 20 wt%) were immersed in Minimum Essential Medium (MEM) containing 10% fetal bovine serum at 37 °C for 72 h, with the ratio of sample to medium 1 g/ml. Besides a blank control, high density polyethylene was set as the negative control, penicillin and streptomycin was set as the positive control. After that, the cell culture medium of L-929 in 96-well plates (10^4 cells per well) for 24 h was removed, replaced with 25%, 50%, 75%, 100% sample extract, positive and negative control extract respectively, then cultured in cell incubator (37 °C, 5% CO_2, humidity > 90%) for 24 h. After the culture, the cell morphology and cell lysis were observed under microscope, and the cell viability value of the test
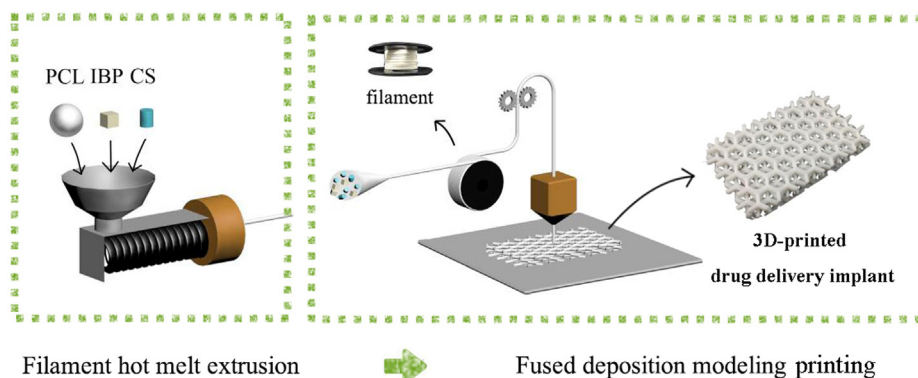
Fig. 1. Schematic diagram of implant fabrication.

Table 2
The optimized printing parameters used in FDM.

Processing variables		Values
Temperature (°C)	Printing nozzle temperature	120
	Platform temperature	0
Speed (mm/s)	Printing speed	60
	Traveling speed	100
	Bottom printing speed	20
	Outer wall printing speed	30
	Inner wall printing speed	60
Quality (mm)	Layer height	0.2
	Wall thickness	0.8
	Bottom/top layer thickness	0.6
	Fill density (%)	20
	Extrusion capacity (%)	100
	Double extrusion overlap	0.15
	Minimum layer cooling time (s)	5
Nozzle diameter (mm)		0.8

article was measured by methyl thiazolyl tetrazolium (MTT) assay method. There were six replicates in each group.

3. Results and discussion

3.1. Printability of the filaments

Filament with appropriate mechanical properties is the premise of the FDM process. The thermoplastic filament was forced into the heating nozzle through a pair of counter-rotating gears. Hence it was necessary to ensure that the filament could pass through the gears continuously and smoothly. Therefore, the filaments were subjected to tensile tests to investigate their tensile strength. The influence of the drug content on tensile strength is shown in Fig. 2a. The tensile strength decreased when the drug content was higher, indicating that the filament stiffness decreased linearly upon plasticization by adding more IBP ($y = -0.541x + 15.167$, $R^2 = 0.9214$). The addition of a drug weakened the intermolecular forces of PCL, causing its tensile properties to decline. In the same way, the tensile strength was inversely correlated with the CS content ($y = -0.378x + 11.93$, $R^2 = 0.9936$), as displayed in Fig. 2b. As the CS content increased, the stress concentration increased. CS acted as a plasticizer that weakened the intermolecular forces of the PCL matrix and decreased the degree of interchain entanglement, which ultimately decreased the tensile strength of the material. Furthermore, the gear motion in the process of feeding filaments to the FDM printer was tested. The filaments possessed relatively high σ_t and could be smoothly driven by the gears.

The rheological behavior of the filament also heavily influences the FDM process. Only the filament with appropriate viscoelastic-ity can be extruded smoothly by the FDM nozzle and solidified instantly when printing each layer. As illustrated in Fig. 2c, and 2d, the presence of IBP reduced the complex viscosity and storage modulus of PCL. When IBP with a relatively low molecular weight was inserted into PCL chains, the distance between PCL chains increased and the intermolecular forces weakened. The PCL chains stretched and became prone to slip in the material, leading to a plasticizing effect. Similar plasticizing effects of IBP on Kollidon® SR polymer [40] have also been reported. As shown in Fig. 2e, and 2f, the presence of CS also reduced the complex viscosity and storage modulus of PCL but to a lesser extent than IBP. This might be explained as the difference in structures between IBP and CS. The polarity of CS, with many hydroxyl groups, is greater than that of PCL, which has more ether bonds and ester groups. Therefore, based on the "like dissolves like" principle, the compatibility of IBP and PCL was better, and IBP was better dispersed in the PCL matrix. As a result, the intermolecular forces were weakened, and the complex viscosity and storage modulus decreased faster. Moreover, the complex viscosity of all composites decreased upon increasing the frequency, showing shear thinning behavior, which allowed the filament melt to pass through the nozzle smoothly. In summary, the addition of IBP and CS improved the plasticity of PCL; a low filler content must be used to meet the demands of filaments during the FDM printing process. All filaments could be processed using FDM in this experiment.

3.2. Changes before and after HME and FDM processes

The binding strength of the phases in filaments had a great impact on the final properties of the printed composite structures, and the binding strength was determined by the intermolecular interactions of each phase. The FTIR spectra of the samples are shown in Fig. 3a. The FTIR spectrum of PCL showed several bands corresponding to the CH_2 symmetric stretch at 2944 cm^{-1}, CH_2 asymmetric stretch at 2865 cm^{-1}, carbonyl stretch at 1720 cm^{-1}, C-O and C-C stretch at 1290 cm^{-1}, and C-O-C asymmetric stretch at 1240 cm^{-1}. The drug was represented by the carbonyl stretch at 1710 cm^{-1}. The benzene ring stretch appeared from 1600 cm^{-1} to 1450 cm^{-1}, and the characteristic = C-H stretch of the benzene ring was observed at 2960 cm^{-1}. In terms of CS, the significant peak from 3000 cm^{-1} to 3500 cm^{-1} represented the stretching vibration of O-H and N-H, The peaks appeared at 2889 (-CH stretching) and 1659 cm^{-1} (amide I). In the 3D-printed implant spectrum, some peaks shifted. A broad band from 3000 cm^{-1} to 2500 cm^{-1} appeared, which indicated the formation of strong hydrogen bonds between the unique carboxyl group of IBP and the hydroxyl group of PCL. Additionally, the formation of hydrogen bonds homogenized the electron cloud density, which reduced the frequency of the stretch.
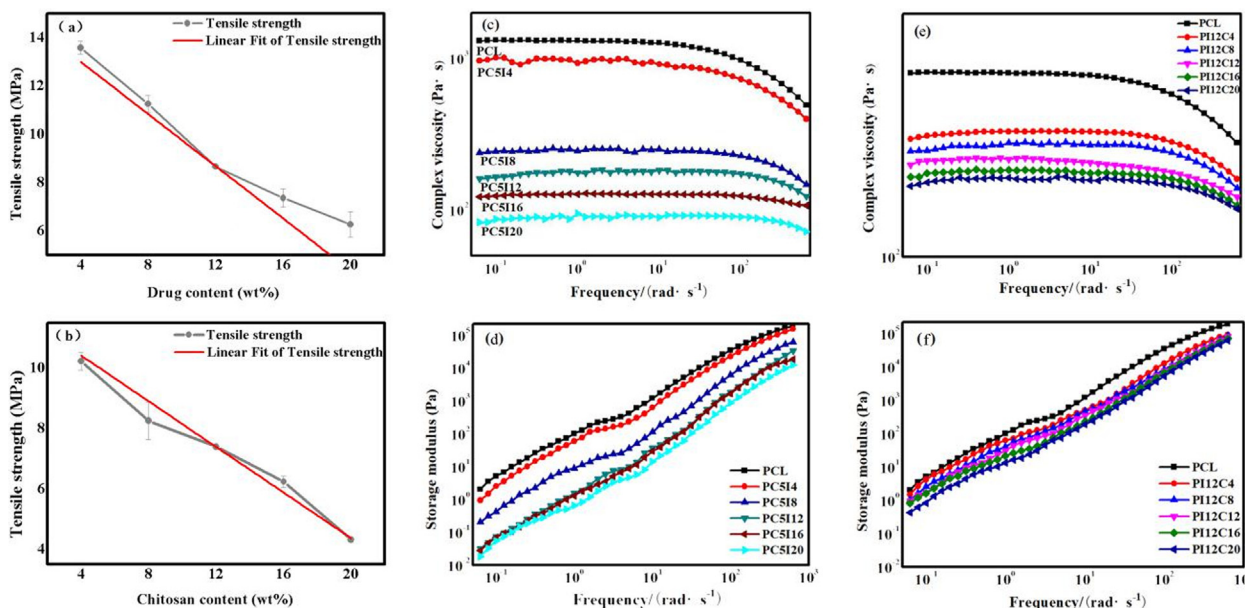
Fig. 2. Influence of (a) drug content and (b) CS content on tensile strength (σ_t) at the break of filaments. The relationship between frequency and (c and e) complex viscosity (η^*), (d and f) storage modulus (G') of filaments.
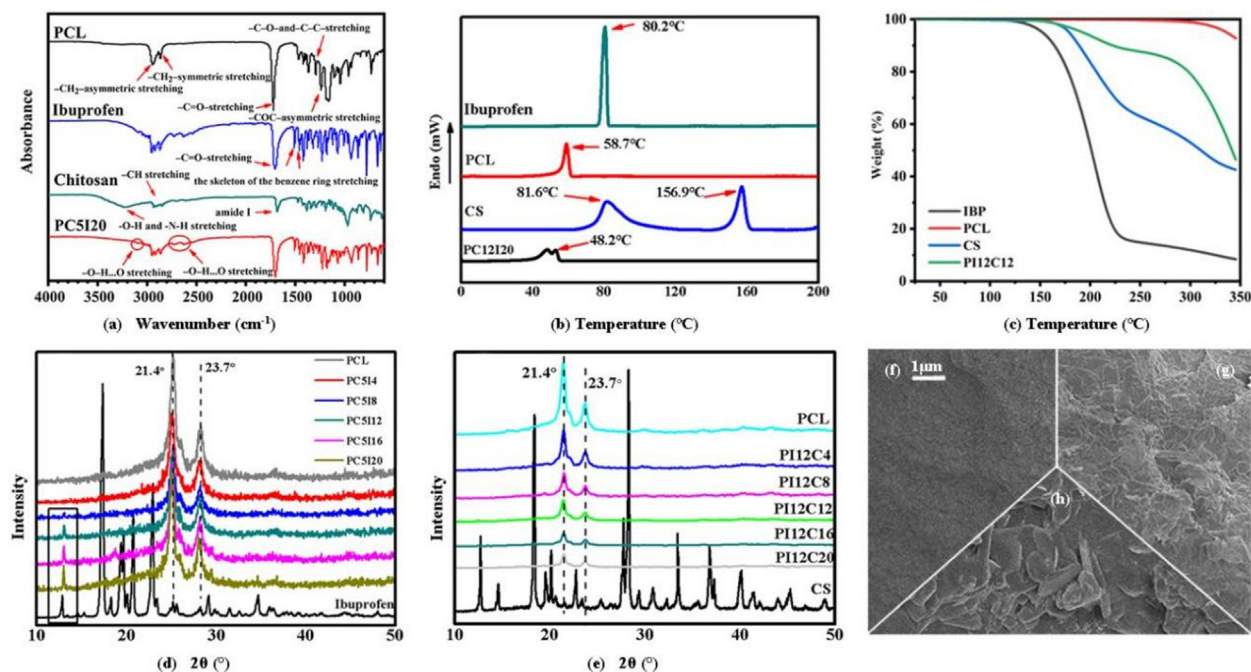

Fig. 3. (a) FTIR spectra of PCL, IBP, CS and 3D-printed implants. (b) DSC patterns of PCL, IBP, CS, and 3D-printed implants. (c) TG patterns of IBP, PCL, CS, and 3D-printed implant. (d),(e) XRD patterns of PCL, IBP, CS, and 3D-printed implants. (f), (g), (h) SEM photograph of 3D-printed implants with an IBP loading of 12 wt% and a CS loading of 4 wt%, 12 wt%, and 20 wt%.

In the spectrum of the 3D-printed implant, the absorption frequency of C=O shifted from 1720 cm^{-1} to a lower wavenumber of 1710 cm^{-1}, further demonstrating the formation of hydrogen bonds. Moreover, no characteristic absorption peak of the drug was observed in the infrared spectrum of the composite material, and no obvious difference was found between the characteristic peak of the drug and the matrix. This indicated that the addition of the drug did not affect the chemical structure of the matrix, and no new chemical bonds were formed during the HME and FDM processes. IBP remained stable at 120 °C, as reported in recent

studies [41,42]. The peak of CS from 3000 cm^{-1} to 3500 cm^{-1} was weakened, which might be due to the decomposition of hydroxyl groups by heat treatment during FDM and HME process.

Beside the changes in the functional groups, the crystalline state of the drug, CS, and PCL might change during the HME and FDM processes. To verify crystallinities, the raw materials and composites were characterized using DSC. As shown in Fig. 3b, the melting point of IBP was 80.2 °C, which demonstrated the presence of drug crystals, consistent with a previous study by Chow [43]. In the CS curve, two relatively smooth endothermic peaks appeared at

81.6 °C and 156.9 °C. The DSC curve of PCL showed an endothermic peak at approximately 58.7 °C, representing the melting point of its known semi-crystalline form. Differences in the thermal behavior were found between the PCL loaded with IBP, CS, and raw materials. The ternary composite containing 20% IBP did not exhibit three endothermic peaks, indicating that their crystalline states changed during HME and printing, which revealed that IBP and CS transformed from crystalline into amorphous materials. The melting point of PCL decreased to 48.2 °C because the addition of the drug and CS played an important role in plasticizing the matrix. Both molecules inserted into the PCL macromolecular chains reduced the crystallinity and weakened the intermolecular forces of PCL. In addition, hydrogen bonds were formed between the PCL chains and the drug, which was also confirmed by the rheology and FTIR results. Thus, the thermal processing window of PCL was broadened.

XRD experiments were carried out to obtain the crystalline structure information of as-received drug powders and PCL/IBP/CS composites containing different amounts of IBP and CS so as to investigate further the crystalline morphology of IBP and CS in composites. The crystallization peaks of PCL and IBP appeared between 10° and 40°, which were consistent with previous reports [44,45]. Pure PCL, as a semi-crystalline material, displayed two obvious characteristics. Bragg diffraction peaks at 2θ values of 21.4° and 23.7°. These were respectively attributed to the (110) and (200) lattice planes, indicating that PCL retained its semi-crystalline state after extrusion and printing. The as-received drug powders were confirmed to be stable crystalline, IBP with main peaks at 12.3°, 16.7°, 19.04°, 20.1°, and 22.36° (Fig. 3d). The diffraction peak intensities of PCL in the composites markedly decreased upon increasing the drug loading, indicating a lower crystallinity. At the same time, an extra weak crystallization peak was observed at 2θ = 12.3°, which corresponded to the characteristic peaks of the drug in the XRD diffractogram of the composite containing 8% drug. The weak diffraction peak intensity of the drug in the composites tended to slightly increase as the drug content increased, demonstrating the presence of a few drug crystals in the composites, while most of the crystalline forms of the drug were destroyed during HME and printing. No peak shift was observed upon increasing the drug loading, indicating that the melt processing did not change the crystal structure of PCL. Compared with PCL, CS is a weakly crystalline material present at less than 5% in the composite materials; therefore, its diffraction peak was not observed in the XRD patterns. Moreover, as shown in Fig. 3e, the PCL diffraction peak decreased continuously upon increasing the CS content. The presence of CS influenced the interactions between PCL molecules, which affected the regular arrangement of PCL molecules and reduced its crystallinity. The XRD diffractogram of the composites containing different CS contents showed one characteristic peak of CS, indicating that CS might transform into an amorphous state during HME and FDM.

The TG test was performed to verify the degradation through the whole process. The result showed that under the highest temperature of 120 °C in HME and FDM process, the remaining weight of PCL was 100%, the drug IBP was 99.48%, CS was 99.6% and the final implant (PI12C12) was 99.92%. The onset temperature of PCL was around 333 °C, IBP was 152 °C, CS was 178 °C and implant was 191 °C. Which was far more than 120 °C. Therefore, it came to the conclusion that no obvious degradation occurred in HME and FDM process.

The morphology of the implant was observed using SEM to visually analyze the dispersion of the drug and CS in the PCL matrix. As shown in Fig. 3f, g, h, drug particles were embedded in the PCL matrix, and no obvious agglomeration was detected at a drug loading of 12%, indicating good interfacial adhesion and compatibility between the IBP and PCL matrices. This might be

due to the effect of shear forces on the composites during HME and FDM. In addition, the strong hydrogen bonds between IBP and PCL also improved the interfacial compatibility to some degree, as shown by the FTIR results. A slight local uplift was observed on the surface upon increasing the CS content, but CS particles were not observed. CS increased the roughness of the surface of the implant, but CS was uniformly distributed in the PCL matrix because the single-screw extruder and printer sheared the composite. The addition of CS also reduced the crystallinity of the composite, and hence CS and PCL matrix were well fused.

3.3. Drug release behavior

A study of the release behavior of the implant is necessary for its application. The structure of the implant greatly influenced the release performance. Fig. 4a compared the accumulated release over time of two structures as an example. Two different structures (structure 1 and structure 2) with the same size, CS content of 12 wt%, and IBP content 12 wt% were printed. Both structure 1 and structure 2 had three layers, but structure 2 was interlaced between two layers, and structure 1 was denser than structure 2. The slope of the release line of structure 2 was higher, indicating a faster release rate. The accumulative release from structure 2 increased from 43% to 62.3% compared with structure 1. This was likely because structure 2 had a much higher relative specific surface area, and the drug was more exposed to the PBS buffer solution, which promoted a more complete and efficient release. As a result, the drug release could be controlled by adjusting the structure and shape of the implant, which could be easily realized by 3D printing.

The influence of the drug content (4 wt% to 20 wt%) with structure 2 on *in vitro* dissolution is shown in Fig. 4b. The drug release increased from 28% to 100% when the drug content increased from 4% to 20%. The dissolution of the drug introduced more release channels in the PCL matrix, leading to complete drug release.

The influence of the CS content with structure 2 on the drug release behavior is shown in Fig. 4c. The drug release increased from 55% to 100% when the CS content increased from 4% to 20%. With higher CS contents, both the rate and extent of drug release increased because more release channels were formed, leading to an easy and complete release of the drug. The change was obvious from CS contents of 4 wt% to 12 wt%, but the accumulative release rate did not obviously change upon increasing the CS content. This might be due to the limited drug dosage, which led to the upper limit of drug release. Too much CS affected the printability of the filament, as described in Section 3.1. As a result, a proper amount of CS should be added to form enough channels without destroying the printing performance of the filament.

In summary, depending on the patients' need, a controllable accumulative release could be achieved at a specific time by changing the drug and CS contents and structures.

3.4. Drug release mechanism

When designing an implantable drug delivery device, it is necessary to focus on the mechanism(s) and hence the kinetics of release of the desired drug. In order The *in vitro* drug release data of 3D-printed implants were fitted by zero-order, first-order, and Ritger-Peppas mathematical models to determine the drug release mechanism. The correlation coefficient R^2 was chosen as the reference to define the approximation accuracy of each model. As shown in Table 3, the first-order and Ritger-Peppas models fit the data better. The best fit was obtained with the first-order equation ($R^2 > 0.98$ for all samples), indicating that diffusion is the predominant release mechanism of the drug. The Ritger-Peppas
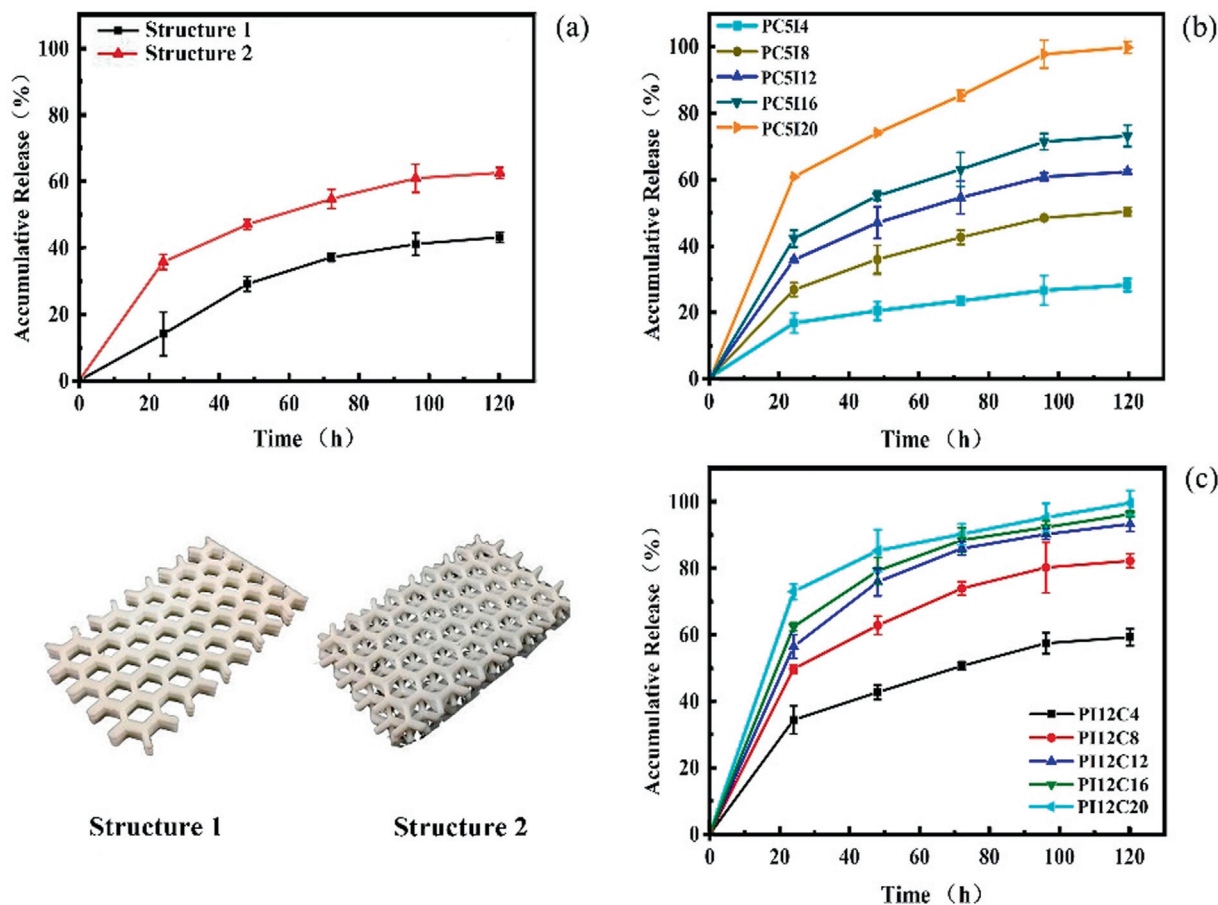
Fig. 4. Influence of (a) the structure, (b) drug content, and (c) CS content on the accumulative release over time.

Table 3
Drug release data fitted using dynamic models.

	Zero order $Mt/M\infty=k_0t + Q_0$	First order $ln(1-Mt/M\infty) = -kt$	Ritger -Peppas $Mt/M\infty=kt^n$	
	R^2	R^2	n	R^2
PI12C4	0.9617	0.9848	0.45	0.9745
PI12C8	0.9044	0.9921	0.63	0.9584
PI12C12	0.8725	0.9986	0.62	0.9438
PI12C16	0.8970	0.9960	0.57	0.9243
PI12C20	0.9451	0.9910	0.49	0.8691

equation showed that the drug release also proceeded via a diffusion-erosion mechanism (0.45 < n < 0.89).

The SEM images further verified the drug release mechanism. The surfaces of the printed implants before and after the release are shown in Fig. 5. Taking the CS content of 12% as an example, compared with the CS content of 4%, small channels were found on the surface of the structures after implant soaking, as shown in Fig. 5f, which were caused by the dissolution of water-soluble CS. The number of channels increased upon increasing the CS content, which facilitated further drug release, leading to an improvement in the total drug release amount and efficiency. The drug was released gradually, and CS eroded slowly. This observation was consistent with the diffusion-erosion drug release mechanism indicated by the data fitting with the Ritger -Peppas model. As shown in Fig. 6, the drug on the surface of the implant rapidly dissolved in the buffer solution immediately after dipping the sample into the release medium in the first stage. This was called the "burst effect", which was explosive dissolution, and the drug was mainly released via a diffusion mechanism in this stage. This was

accompanied by the dissolution of some of the CS, which formed a small number of pores on the surface. In the second stage, as time went on, the drug on the surface of the implant diffused into the solution, and more CS was exposed to the buffer solution, causing further dissolution. This led to the formation of more pore channels on the surface of the implant, and more drug was released through these channels. At this time, the release method of the drug was a combination of free diffusion and erosion. In the third stage, the drug on the surface of the implant was nearly completely dissolved, and a large number of pores were formed due to the dissolution of a large amount of CS, so that the number of drug release channels increased. As a result, the drug was mainly released through the channels, and in this stage, the drug was mainly released via an erosion mechanism.

3.5. Cytotoxicity of the implant

Implants are required to have good compatibility with human body. Although PCL and CS are products with good biocompatibility,
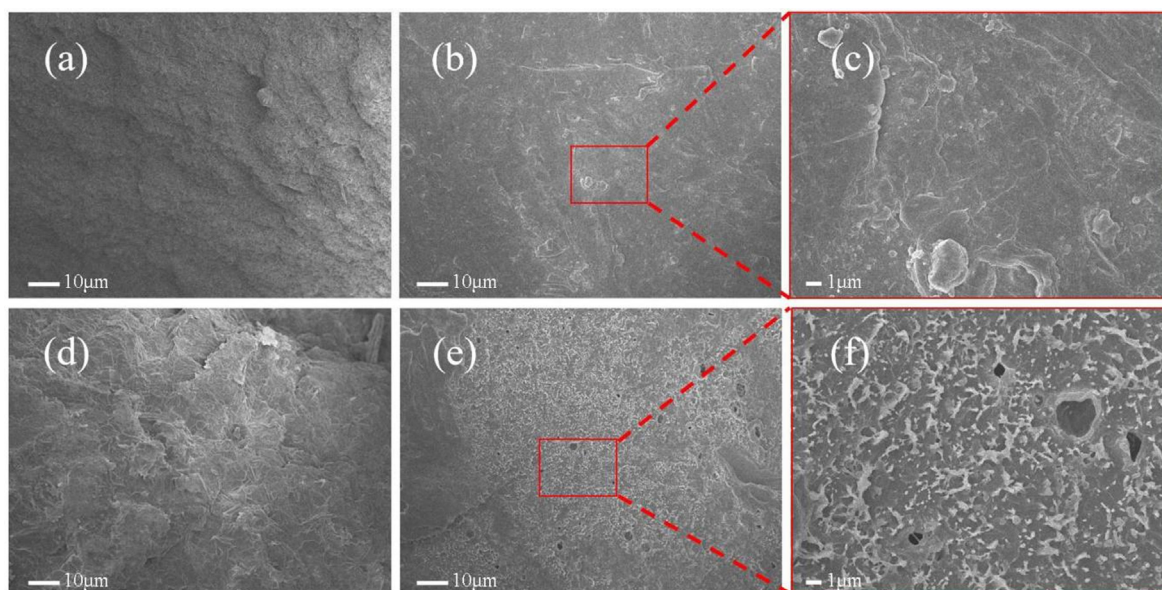
Fig. 5. SEM images of the surfaces of 3D-printed structures with different CS loadings before and after release: (a) 4 wt%, (d) 12 wt%, corresponding to (b), (e) and (c) and (f) are the local amplification of (b) and (e) respectively.
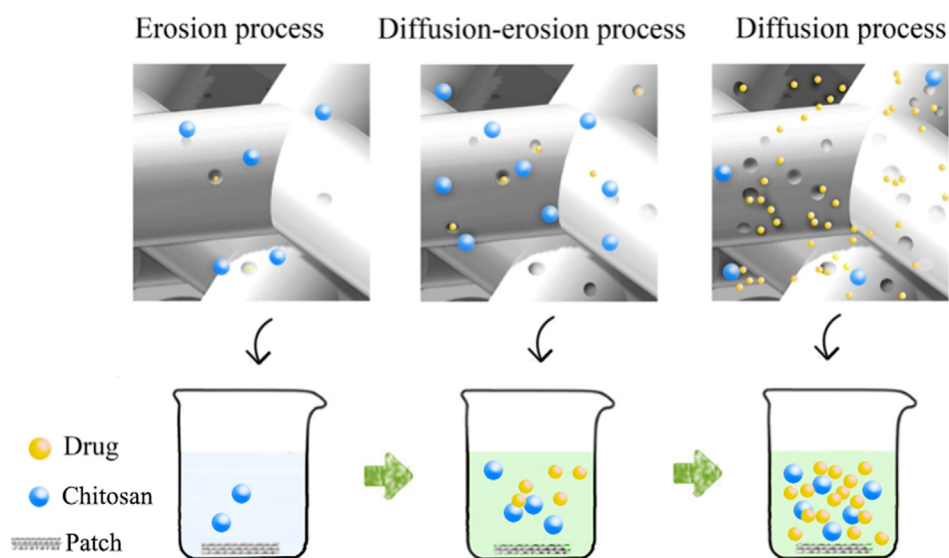

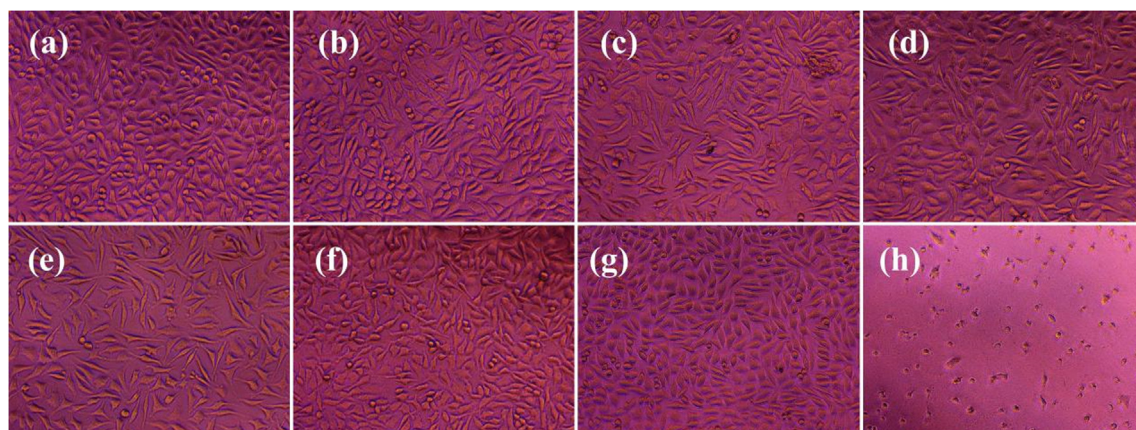**Fig. 6.** Schematic diagram of the drug release process.

Fig. 7. Morphology under optical microscope of (a) 25% implant extract; (b) 50% implant extract; (c) 75% implant extract; (d) 100% implant extract; (g) negative control: high density polyethylene extract; (h) positive control: penicillin and streptomycin cultured L-929 cell and the blank control before (e) and after (f) culture.

the HME and FDM processes may affect the biocompatibility of the final products. Therefore, the cytotoxicity of the implant was tested. As shown in Fig. 7, the cell morphology of the blank control before and after culture and negative control was almost the same, the cell in active control group changed greatly, indicating the decrease of cell viability. In contrast, the cell morphology of the implant group was basically intact after incubating the cells for 24 h, which should be attributed to the biocompatible materials and the harmless processing methods. The MTT results also verified the biocompatibility of the implant, the cell viability value of blank control and negative control was 100%, positive control was 9.2. 25%, 50%, 75%, 100% implant extract was 94.37%, 87.4%, 84.0%, 75.3% (Table S1), respectively, showing a preferable biocompatibility.

4. Conclusions

In this study, a biocompatible, complex-shaped, sustained drug release implant based on PCL and CS was achieved by FDM printing without adding organic solvent. All the filament in the paper has good printability. IBP and CS acted as plasticizers that weakened the intermolecular forces of the PCL matrix and decreased the degree of interchain entanglements, which ultimately decreased the tensile strength of the material. This restricted the filler content of the filaments used in FDM printing. The changes in the filaments before and after HME and FDM processes were studied. The FTIR results showed that strong hydrogen bonds were formed between the unique carboxyl group of IBP and the hydroxyl group of PCL, but no new chemical bonds were formed, together with TGA results, indicating that the drug, CS, PCL, did not degrade during HME and FDM processes. The DSC and XRD results showed that most of the crystalline structure of the drug was destroyed during HME and FDM processes, and CS might have transformed into an amorphous state. Both molecules inserted into the PCL macromolecular chains reduced the crystallinity of PCL, and the intermolecular forces of PCL were weakened. Thus, the thermal processing window of PCL was broadened. The morphology was observed using SEM, which showed that the interfacial adhesion and compatibility between the drug and the PCL matrix were good. Although CS increased the surface roughness of the implant, it was well fused with the matrix and uniformly distributed. The release behavior and the mechanism were explored, which showed that the release extent and rate increased at higher CS and drug contents. Notably, controllable and sustained drug release over 120 h was achieved by adjusting the drug and CS contents, as well as the printed structures. The release was well fitted by the first-order and Ritger-Peppas models and verified by SEM. As a result, the released mechanism was shown to be diffusion-erosion. The biocompatibility was measured using MTT assay, the cell was basically intact after implant extract incubating for 24 h, the cell viability value of 100% implant extract was 75.3%, showing a preferable biocompatibility. In conclusion, FDM printing made it possible for implants with different structures and shapes and allowed the drug release to be tailored to the time or dose. Hence, the filament could be manufactured as an implant for controllable and efficient sustained drug release in personalized administration. The sustained drug release implant was also expected to be used as scaffolds or catheters to support the wounds in human body, such as bone tissue repair, facial plastic surgery.

Declaration of Competing Interest

The authors declare that they have no known competing financial interests or personal relationships that could have appeared to influence the work reported in this paper.

Data availability statement

The raw/processed data required to reproduce these findings cannot be shared at this time as the data also forms part of an ongoing study.

Appendix A. Supplementary data

Supplementary data to this article can be found online at https://doi.org/10.1016/j.matdes.2022.110394.

References

[1] A. Liaskoni, R.D. Wildman, C.J. Roberts, 3D printed polymeric drug-eluting implants, Int. J. Pharm. 597 (2021) 120330.

[2] M. Alomari, F.H. Mohamed, A.W. Basit, S. Gaisford, Personalised dosing: Printing a dose of one's own medicine, Int. J. Pharm. 494 (2015) 568–577.

[3] A. Santos, M. Sinn Aw, M. Bariana, T. Kumeria, Y.e. Wang, D. Losic, Drug-releasing implants: current progress, challenges and perspectives, J. Mater. Chem. B. 2 (37) (2014) 6157–6182.

[4] F.P. Pons-Faudoa, A. Ballerini, J. Sakamoto, A. Grattoni, Advanced implantable drug delivery technologies: transforming the clinical landscape of therapeutics for chronic diseases, Biomed. Microdevices. 21 (2019) 47.

[5] L. Zema, A. Melocchi, A. Maroni, A. Gazzaniga, Three-dimensional printing of medicinal products and the challenge of personalized therapy, J. Pharm. Sci. 106 (7) (2017) 1697–1705.

[6] B. Tesfamariam, Bioresorbable scaffold-based controlled drug delivery for restenosis, J. Cardiovasc. Trans. Res. 12 (3) (2019) 193–203.

[7] W. Wang, Y. Miao, X. Zhou, W. Chen, L. Chen, D. Liu, H. Du, C. H, Local delivery of BMP-2 from poly(lactic-co-glycolic acid) microspheres incorporated into porous nanofibrous scaffold for bone tissue regeneration, J. Biomed Nanotechnol. 13(2017) 1446-1456.

[8] K. Ahtiainen, L. Sippola, M. Nurminen, B. Mannerström, S. Haimi, R. Suuronen, J. Hyttinen, T. Ylikomi, M. Kellomäki, S. Miettinen, Effects of chitosan and bioactive glass modifications of knitted and rolled polylactide-based 96/4L/D scaffolds on chondrogenic differentiation of adipose stem cells, J. Tissue. Eng. Regen. M. 9 (2015) 55–65.

[9] C. Song, A. Wang, Z. Wu, Z. Chen, Y. Yang, D. Wang, The design and manufacturing of a titanium alloy beak for *Grus japonensis* using additive manufacturing, Mater. Des. 117 (2017) 410–416.

[10] S.J. Trenfield, A. Awad, A. Goyanes, S. Gaisford, A.W. Basit, 3D printing pharmaceuticals: drug development to frontline care, Trends. Pharmacol. Sci. 39 (5) (2018) 440–451.

[11] S.K. Eshkalak, E.R. Ghomi, Y. Dai, D. Choudhury, S. Ramakrishna, The role of three-dimensional printing in healthcare and medicine, Mater. Des. 194 (2020) 108940.

[12] Y. Hu, R.B. Ladani, M. Brandt, Y. Li, A.P. Mouritz, Carbon fibre damage during 3D printing of polymer matrix laminates using the FDM process, Mater. Des. 205 (2021) 109679.

[13] Z. Tan, T. Liu, J. Zhong, Y. Yang, W. Tan, Control of cell growth on 3D-printed cell culture platforms for tissue engineering, J. Biomed. Mater. Res. A. 105 (12) (2017) 3281–3292.

[14] M. Mantecón-Oria, N. Diban, M.T. Berciano, M.J. Rivero, O. David, M. Lafarga, O. Tapia, A. Urtiaga, Hollow fiber membranes of PCL and PCL/graphene as scaffolds with potential to develop in vitro blood - brain barrier models, Membranes. 10 (2020) 161.

[15] M. Ranjbar-Mohammadi, M.P. Prabhakaran, S.H. Bahrami, S. Ramakrishna, Gum tragacanth/poly(l-lactic acid) nanofibrous scaffolds for application in regeneration of peripheral nerve damage, Carbohydr. Polym. 140 (2016) 104–112.

[16] S. Mombini, J. Mohammadnejad, B. Bakhshandeh, A. Narmani, J. Nourmohammadi, S. Vahdat, S. Zirak, Chitosan-PVA-CNT nanofibers as electrically conductive scaffolds for cardiovascular tissue engineering, Int. J. Biol. Macromol. 140 (2019) 278–287.

[17] A. Allafchian, H. Hosseini, S.M. Ghoreishi, Electrospinning of PVA-carboxymethyl cellulose nanofibers for flufenamic acid drug delivery, Int. J. Biol. Macromol. 163 (2020) 1780–1786.

[18] M. Brzeziński, M. Socka, B. Kost, Microfluidics for producing polylactide nanoparticles and microparticles and their drug delivery application, Polym. Int. 68 (6) (2019) 997–1014.

[19] M. Korang-Yeboah, Y. Gorantla, S.A. Paulos, P. Sharma, J. Chaudhary, R. Palaniappan, Polycaprolactone/maltodextrin nanocarrier for intracellular drug

delivery: formulation, uptake mechanism, internalization kinetics, and subcellular localization, Int. J. Nanomed. 10 (2015) 4763–4781.

[20] A. Goyanes, M. Kobayashi, R. Martínez-Pacheco, S. Gaisford, A.W. Basit, Fused-filament 3D printing of drug products: Microstructure analysis and drug release characteristics of PVA-based caplets, Int. J. Pharm. 514 (2016) 290–295.

[21] N. Genina, J. Holländer, H. Jukarainen, E. Mäkilä, J. Salonen, N. Sandler, Ethylene vinyl acetate (EVA) as a new drug carrier for 3D printed medical drug delivery devices, Eur. J. Pharm. Sci. 90 (2016) 53–63.

[22] W. Jamróz, M. Kurek, A. Czech, J. Szafraniec, K. Gawlak, R. Jachowicz, 3D printing of tablets containing amorphous aripiprazole by filaments co-extrusion, Eur. J. Pharm. Biopharm. 131 (2018) 44–47.

[23] N.G. Solanki, M. Tahsin, A.V. Shah, A.T.M. Serajuddin, Formulation of 3D printed tablet for rapid drug release by fused deposition modeling: screening polymers for drug release, drug-polymer miscibility and printability, J. Pharm. Sci. 107 (2018) 390–401.

[24] H. Öblom, J. Zhang, M. Pimparade, I. Speer, M. Preis, M. Repka, N. Sandler, 3D-printed isoniazid tablets for the treatment and prevention of tuberculosis-personalized dosing and drug release, AAPS. PharmSciTech. 20 (2019) 52.

[25] I. Serris, P. Serris, K.M. Frey, H. Cho, Development of 3D-printed layered PLGA films for drug delivery and evaluation of drug release behaviors, AAPS. PharmSciTech. 21 (2020) 256.

[26] B.S. Jang, J.E. Jeong, S. Ji, D. Im, M.K. Lee, S.A. Park, W.H. Park, Advanced stent applications of material extrusion 3D printing for palliative treatment of unresectable malignant hilar biliary obstruction, Mater. Des. 195 (2020) 109005.

[27] G. Wu, X. Ma, L. Fan, Y. Gao, H. Deng, Y. Wang, Accelerating dermal wound healing and mitigating excessive scar formation using LBL modified nanofibrous mats, Mater. Des. 185 (2020) 108265.

[28] S.A. Park, S.J. Lee, J.M. Seok, J.H. Lee, W.D. Kim, I.K. Kwon, Fabrication of 3D printed PCL/PEG polyblend scaffold using rapid prototyping system for bone tissue engineering application, J. Bionic. Eng. 15 (3) (2018) 435–442.

[29] J. Holländer, N. Genina, H. Jukarainen, M. Khajeheian, A. Rosling, E. Mäkilä, N. Sandler, Three-dimensional printed PCL-based implantable prototypes of medical devices for controlled drug delivery, J. Pharm. Sci. 105 (9) (2016) 2665–2676.

[30] S. Sahoo, A. Sasmal, R. Nanda, A.R. Phani, P.L. Nayak, Synthesis of chitosan–polycaprolactone blend for control delivery of ofloxacin drug, Carbohydr. Polym. 79 (1) (2010) 106–113.

[31] Y.M. Than, V. Titapiwatanakun, Tailoring immediate release FDM 3D printed tablets using a quality by design (QbD) approach, Int. J. Pharm. 599 (2021) 120402.

[32] H.R. Munj, J.J. Lannutti, D.L. Tomasko, Understanding drug release from PCL/gelatin electrospun blends, J. Biomater. Appl. 31 (6) (2017) 933–949.

[33] B. Chen, Y. Wang, X. Tuo, Y. Gong, J. Guo, Tensile properties and corrosion resistance of PCL-based 3D printed composites, J. Appl. Polym. Sci. 138 (2021) 50253.

[34] D.R. Fonseca, R. Sobreiro-Almeida, P.C. Sol, N.M. Neves, Development of non-orthogonal 3D-printed scaffolds to enhance their osteogenic performance, Biomater. Sci. 6 (6) (2018) 1569–1579.

[35] M. Kyobula, A. Adedeji, M.R. Alexander, E. Saleh, R. Wildman, I. Ashcroft, P.R. Gellert, C.J. Roberts, 3D inkjet printing of tablets exploiting bespoke complex geometries for controlled and tuneable drug release, J. Control. Release. 261 (2017) 207–215.

[36] D. Liu, W. Nie, D. Li, W. Wang, L. Zheng, J. Zhang, J. Zhang, C. Peng, X. Mo, C. He, 3D printed PCL/SrHA scaffold for enhanced bone regeneration, Chem. Eng. J. 362 (2019) 269–279.

[37] L. Dai, T. Wu, Z. Wang, R. Yuan, Y. Ding, W. Zhang, S. Chu, S. Ju, J. Yu, Ibuprofen-mediated potential inhibition of biofilm development and quorum sensing in *Pseudomonas aeruginosa*, Life. Sci. 237 (2019) 116947.

[38] S. Shehata, C.J. Serpell, S.C.G. Biagini, Architecture-controlled release of ibuprofen from polymeric nanoparticles, Mater. Today. Commun. 25 (2020) 101562.

[39] Y. Mao, M. Chen, R. Guidoin, Y. Li, F. Wang, G. Brochu, Z. Zhang, L. Wang, Potential of a facile sandwiched electrospun scaffold loaded with ibuprofen as an anti-adhesion barrier, Mater. Sci. Eng. C. 118 (2021) 11451.

[40] I. Özgüney, D. Shuwisitkul, R. Bodmeier, Development and characterization of extended release Kollidon SR mini-matrices prepared by hot-melt extrusion, Eur. J. Pharm. Biopharm. 73 (1) (2009) 140–145.

[41] K. Shi, J.P. Salvage, M. Maniruzzaman, A. Nokhodchi, Role of release modifiers to modulate drug release from fused deposition modelling (FDM) 3D printed tablets, Int. J. Pharm. 597 (2021) 120315.

[42] T. Ehtezazi, M. Algellay, Y. Islam, M. Roberts, N.M. Dempster, S.D. Sarker, The application of 3D printing in the formulation of multilayered fast dissolving oral films, J. Pharm. Sci. 107 (4) (2018) 1076–1085.

[43] S.F. Chow, M. Chen, L. Shi, A.H.L. Chow, C.C. Sun, Simultaneously improving the mechanical properties, dissolution performance, and hygroscopicity of ibuprofen and flurbiprofen by cocrystallization with nicotinamide, Pharm. Res. 29 (7) (2012) 1854–1865.

[44] S. Ishihara, Y. Hattori, M. Otsuka, MCR-ALS analysis of IR spectroscopy and XRD for the investigation of ibuprofen - nicotinamide cocrystal formation, Spectrochim. Acta. A. Mol. Biomol. Spectrosc. 221 (2019) 117142, https://doi.org/10.1016/j.saa.2019.117142.

[45] Y. Xu, Y. Xiong, S. Guo, Effect of liquid plasticizers on crystallization of PCL in soft PVC/PCL/plasticizer blends, J. Appl. Polym. Sci. 137 (2019) 48803.